RESEARCH ARTICLE

Pathway-Selection for Programmable Assembly of Genetically Encoded Amphiphiles by Thermal Processing

Masoumeh Khodaverdi,[a] Md Shahadat Hossain,[a] Zhe Zhang,[a] Robert P. Martino,[a] Connor W. Nehls,[a] and Davoud Mozhdehi*[a][b]

[a] M. Khodaverdi, M. S. Hossain, Z. Zhang, R. P. Martino, C. W. Nehls, Prof. Dr. D. Mozhdehi
Department of Chemistry
Syracuse University
Center for Science and Technology, 111
dmozhdeh@syr.edu

[b] Prof. Dr. D. Mozhdehi
BioInspired Syracuse: Institute for Material and Living Systems
Syracuse University,
Syracuse, NY 13244, USA

Supporting information for this article is given via a link at the end of the document.

Abstract: Engineering the fate of supramolecular assemblies by heat treatment (i.e., using thermal preparative pathways) remains challenging and a largely ad hoc process. The rational design of such trajectories requires precise manipulation of the strength of molecularly encrypted interactions along an assembly path defined by changes in free energy as a function of temperature. Here, we use temperature-triggered liquid-liquid phase separation of proteins to program the nano- and meso-scale assembly of a genetically encoded amphiphile—a post-translationally lipidated protein— along user-defined thermal trajectories. This molecularly defined pathway was used to funnel thermal energy into the system to direct building blocks to a previously inaccessible region of the energy landscape, and to synthesize two-dimensional nanomaterials with sophisticated structures such as braids and toroids. Because proteins' phase boundaries and transition are programmable at the sequence-level, our strategy opens new horizons to expand the structural hierarchy and functional landscape of protein-based materials.

Introduction

Programming the hierarchical organization of supramolecular assemblies offers promising opportunities for the design of functional materials.[1] At the molecular level, programming often involves engineering deep energy minima to sculpt the shape of the energy landscape, which controls the hierarchical organization of the assemblies.[2] This is achieved by encoding competing interactions in the covalent framework of the molecules and leveraging the difference in how these forces scale with *distance (molecular coordinates)* to control the equilibrium geometry.[3] This approach, however, is best suited for thermodynamically favored assemblies; and less so for kinetically-trapped[4] and adaptable assemblies.[5] Also since assembly instructions are only included in the building blocks' chemical structure, altering their supramolecular assembly and function requires costly and time-consuming synthetic manipulation of building blocks.

To access assemblies with distinct forms and functions from the same building blocks, the order or type of *processing steps* (i.e., the preparative pathways) can be changed to direct molecular building blocks to different regions of the energy landscape.[6] Specifically, changes to an *operating parameter* are used to modify the free energy landscape along the user-defined assembly *trajectory* by modulating programmable attractive and repulsive interactions that determine the hierarchical organization (Figure 1a). Pathway-dependent control over the structure and function of supramolecular assemblies can be achieved by i) funneling energy (chemical, thermal, etc.) into the system at defined time/composition coordinates[5, 7]; or ii) modulating solution operating parameters such as ionic strength,[8] pH,[9] solvent composition,[9b, 10] etc.[11] during the sample preparation.

Modifying the free energy landscape by modifying temperature (thermal processing) offers unique advantages such as high-resolution spatial/temporal control and rapid reversibility, which are absent from chemical processing methods.[11a, 12] Consequently, heat treatment is frequently used as a materials processing method to improve properties of condensed and soft materials, (e.g., hardening of alloys[13] and controlling the nano-morphology of polymers[14]). However, use of this strategy to control nano- and meso-scale assemblies of biomacromolecules such as proteins has been hampered by the incomplete understanding of the temperature dependence of competing interactions (e.g., ionic, H-bond, etc.) that govern the proteins' structure and supramolecular assembly as well as the difficulty in accounting for entropic and solvation contributions in water.[15] Despite the progress in our understanding of the thermodynamic assembly of concentrated protein solutions,[16] the design of protein-based assemblies that can traverse complex thermal trajectories in a programmable manner and yield structurally diverse nano-assemblies remains challenging.

To overcome these challenges, we designed a hybrid protein-based amphiphile with two domains that exhibit different temperature-dependent interaction potentials due to their distinct physicochemistry. The net attractive/repulsive interactions of each domain with itself or solvent can be measured and quantitatively described using solution thermodynamic parameters as a function of temperature (e.g., second virial coefficients[17] or interaction parameters[18]). This information can then be integrated into the molecular design of building blocks to enable programmable navigations of assemblies on the energy landscape by changing the operating parameter (temperature)

We hypothesized that judicious choice of thermal processing rate (i.e., quenching or annealing) enables the control of the assemblies' structural hierarchy by accessing configurations outside of thermodynamic equilibrium (Figure 1a).

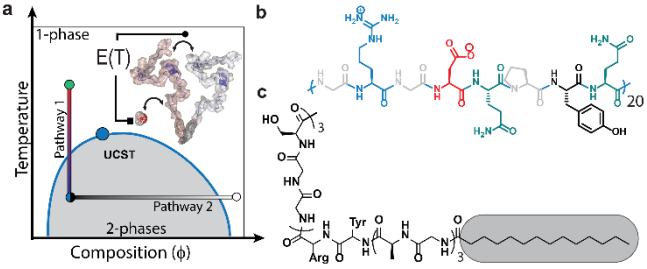

Figure 1. (**a**) The self-assembly of a model supramolecular building block— a genetically encoded amphiphile—is governed by the topology of its energy landscape which is a function of molecularly encoded competing interactions and how they scale with molecular coordinates. User-defined modulation of competing interactions along an assembly path, defined by changes in the free energy as a function of operating parameter such as temperature (T), enables directed assembly of building blocks toward new configurations outside of equilibrium-allowed regions. (**b**) The chemical structure of the prototypical UCST polypeptide, RIP, contains flexible and structure-breaking residues as well as amino acids capable of forming ionic and hydrogen bonds. (**c**) The chemical structure of lipidation domain (the N-terminal peptide fragment). The myristoyl group is highlighted in grey. We note the large due to the large asymmetry between RIP and lipidation domain, this ^{lipo}IDPP integrates the molecular features of both peptide amphiphiles and polymeric surfactants.

Results and Discussion

To demonstrate the feasibility of this approach, we used post-translationally lipid-modified intrinsically disordered protein polymers (^{lipo}IDPPs) to start our design process. Our strategy exploits i) the relative temperature-independence of the hydrophobic effect between 25 °C and 100 °C,[19] and ii) IDPPs' well-documented ability to exhibit sequence-defined temperature-triggered liquid-liquid phase separation (LLPS).[20] The amino acid sequence of IDPP determines how the net attractive/repulsive interactions between polypeptide chains changes in response to increases or decreases in temperature.[21] For example, IDPPs with temperature-sensitive attractive interactions (e.g., H-bond or ionic) between the chains exhibit an upper critical solution temperature (UCST).[22] At elevated temperatures, the interaction of IDPP with water is favored but as the temperature is reduced, the net attractive forces between IDPP chains are increased, resulting in a demixing of the protein solution and formation of an IDPP-rich phase below a critical temperature. We hypothesized that the user-defined thermal trajectories across this thermodynamic phase boundary can be used to manipulate the nano-morphology of polymer-rich aggregates by controlling the kinetics of phase separation. This will enable pathway-dependent control over ^{Lipo}IDPP aggregates to achieve structurally diverse nano-and meso-assemblies from one building block, simply by varying the thermal processing parameters such as the rate of cooling and/or final temperature.

In this work, we selected an IDPP based on the consensus sequence of resilin[23]— a commonly used template for encoding UCST behavior—containing 20 repeats of Gly-Arg-Gly-Asp-Gln-Pro-Tyr-Gln.[24] This octapeptide contains: i) glycine and proline residues that are conformationally flexible and can break the secondary structure to ensure that the polypeptide chain remains disordered and does not form kinetically trapped aggregates even at elevated temperatures; ii) a basic arginine residue and an acidic aspartic acid for ionic interactions; iii) glutamine, a polar uncharged amino acid capable of forming hydrogen bonds; and iv) tyrosine, an aromatic amino acid to promote UCST phase behavior (Figure 1b).[21, 25] We called this IDPP resilin-inspired polypeptide (RIP hereafter).

Short-range hydrophobic interactions—orthogonal to sequence-encoded LLPS—were introduced via lipidation of RIP with myristic acid (C14:0) using a reconstituted lipidation pathway in *E.coli*.[26] To control lipid placement, we coexpressed RIP with the enzyme N-myristoyltransferase (NMT), which catalyzes the addition of a myristoyl group to the N-terminal glycine of a short peptide substrate (GAGAGAYRGGSGGSGGS) fused to RIP (Figure 1c). The lipidated IDPP was purified by leveraging its phase behavior (cold-coacervation) at 20 mgL^{-1} culture.[27] Purified myristoyl-modified protein (M-RIP) was characterized by SDS-PAGE, HPLC, and mass spectrometry (Figure S1-S3).

After molecular characterization, we used FT-IR and circular dichroism (CD) to investigate the effect of lipidation on the global structure, conformation, and interactions of M-RIP. The FT-IR spectra of lyophilized RIP and M-RIP exhibited many similarities such as the presence of broad signals often observed in intrinsically disordered proteins (Figure 2a). However, subtle differences in the shape of peaks in amide I–III regions indicate that myristoylation alters the conformations/interactions of protein domains. For example, RIP spectra contained one single broad peak in amide I region (1600–1700 cm^{-1}) centered around 1637 cm^{-1} (assigned to random coils), while M-RIP spectra in the same region exhibited additional features (shoulders) at 1624 and 1647 cm^{-1}. Consistently, both proteins exhibit the characteristic negative CD signal at ~200 nm (Figure 2b,c and S4), as often observed in disordered proteins. The deconvolution of CD signal only showed a modest decrease (<10%) in the disordered content of M-RIP (Figure S5), within the limit of detection of this technique and the accuracy of deconvolution algorithm. Because the M-RIP sequence is highly asymmetric, and contains high fraction of achiral glycine residues, these results only indicate that lipidation does not globally alter the disordered nature of RIP at the chain level, while subtle alterations in the conformations/interactions of disordered chains cannot be ruled out.

To complement this global (chain-level) view, we then used 1D and 2D NMR techniques to investigate how lipidation modulates the structure and dynamics of the protein domain at the local (residue) level. ^{1}H NMR spectra of RIP and M-RIP in D_2O were similar, confirming that lipidation did not result in a global change in the secondary structure of RIP domains (Figure S6). The most remarkable changes, however, were confined to the methyl side chain of alanine residues (that are only found in the lipidation site), and the alpha protons of aspartic acids (found in the resilin domain). Consistency, we observed large chemical shift perturbations (CSP) for the amide protons of alanine and glycine residues in the lipidation site, $\Delta\delta_{HN}$ measured using ^{1}H-^{15}N heteronuclear single quantum coherence (HSQC), Figure 2d and S7a. In contrast, the CSP for the amino acids found in the resilin domain were close to zero, except for Asp and its neighboring Gln residues (Figure 2d, inset). The magnitude of these $\Delta\delta_{HN}$ CSPs are smaller than reported literature values for changes in the ionization of aspartic acids but the shifts along the nitrogen channel ($\Delta\delta_N$) is consistent with changes in hydrogen bonding (Figure S7b).[28] Together, these experiments provide strong evidence that while RIP and M-RIP remain highly disordered and

conformationally flexible, lipidation alters M-RIP's structure and interactions (e.g., hydrogen bonding) at the local level—specifically the lipidation site, and acidic and polar charged residues.

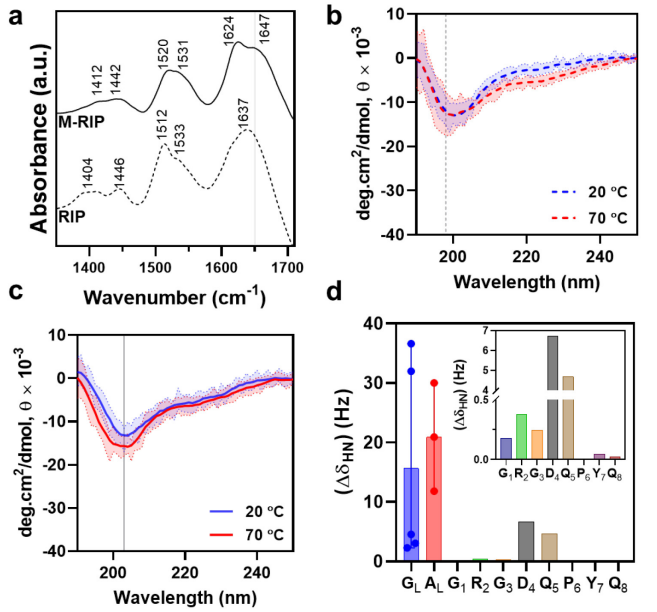

Figure 2. Spectroscopic characterization of the effect of lipidation on the structure and conformation of resilin-derived IDPP. (**a**) Attenuated total reflectance FT-IR spectra of lyophilized RIP and M-RIP showing subtle differences in amide I–III bands. The grey is a visual reference placed at 1650 cm^{-1}, which corresponds to the absorbance of random coils in solution. Variable temperature-CD spectra of (**b**) RIP and (**c**) M-RIP. The shaded area corresponds to standard deviation of signals averaged over 15s at each wavelength. Both RIP and M-RIP exhibit a prominent negative peak centered ~ at 200 nm, which is consistent with the presence of significant disordered domains in both constructs. (**d**) Chemical shift perturbations between HSQC spectra of RIP and M-RIP reported as weighted Euclidean distance $\Delta\delta_{HN}$. The proline residue (an imino acid which forms secondary amides) does not yield a signal in this experiment. The residue numbers correspond to the position of amino acids within the resilin domain, and subscript "L" is used to denote signals from the residues in the lipidation site.

The effect of lipidation on IDPP's UCST thermo-response—binodal coexistence boundaries and reversibility of LLPS—has not been systematically characterized. Therefore, using temperature-programmed turbidimetry, we first mapped the UCST phase-transition boundaries of M-RIP to define the system's operating temperature range. Both M-RIP and the control RIP readily dissolved in deionized water at room temperature (>5% w/v, 2.7 mM). The turbidity of the M-RIP solution increased gradually over the course of 10 min (Figure S8), suggesting that under these conditions, the myristoylated construct undergoes LLPS below room temperature; in contrast the RIP solution remained clear for this period of time. The stock solution was then diluted to the desired concentrations which were subsequently heated to 80 °C and cooled to 20 °C at the rate of ±2 °C min^{-1}. Solution transmittance was measured as a function of temperature during each cycle. Results obtained during the first cooling cycle were combined to generate a 3D contour plot to represent the phase boundaries as functions of temperature and concentration (Figure 3a).

We defined the cloud point, T_{cp} the critical temperature below which the 1-phase solution is no longer stable, as the temperature when the transmittance drops below 35% (schematically shown with a plane separating 1-phase and 2-phase regions). As shown in Figure 3a, M-RIP exhibited a sharp UCST behavior as the turbidity of the solution rapidly increased when the temperature of the solution decreased to below T_{cp} at each concentration. From these results we first conclude that sequence-defined lipidation does not result in an inversion of UCST phase behavior to LCST, contrary to the effect of hydrophobic amino acids shown to promote LCST.[19] Second, given the lack of phase behavior for unmodified RIP (Figure S9) within the tested temperature range (15–70 °C), we conclude that lipidation modulates boundaries between 1-phase and 2-phase regions by increasing the T_{cp} due to the hydrophobicity of the lipid. A similar observation has been reported for synthetic polymers, in which the use of hydrophobic chain ends increases the polymers' UCST cloud point.[29]

We used the cross-section of the 3D surface with the blue plane in Figure 3a to establish a partial temperature-concentration phase diagram (i.e., the coexistence curve which quantifies the dependence of T_{cp} on concentration). The UCST phase boundary of M-RIP depends varies linearly with the natural log of M-RIP solution concentration in the tested regime (Figure S9). The observed UCST phase behavior was reversible (i.e., < 5% change in final turbidity under experimental conditions) over three heating and cooling cycles (Figure 3b). However, the difference measured between the apparent T_{cp} in heating and cooling cycles increased with the rate of heating/cooling (Figure S10). These observations conclusively demonstrate that lipidation modulates the boundaries of the coexistence curve to higher temperatures without sacrificing macroscopic reversibility, a feature advantageous for tuning the LLPS of proteins with extremely low UCSTs, near or even below 0 °C, into biologically relevant temperature ranges.[20a, 30]

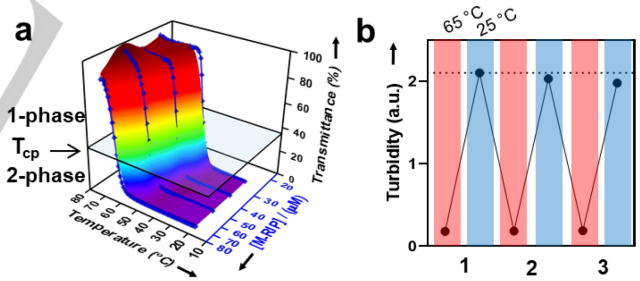

Figure 3. Characterization of M-RIP's thermo-response (UCST phase boundaries and its reversibility). (**a**) 3D contour plot depicts transmittance of M-RIP solution as a function of concentration and temperature. The blue plane schematically represents the T_{cp} and separates 1-phase region from demixed 2-phase solution. The coexistence curve is defined by the intersection of the blue plane and the contour plot. (**b**) The reversibility of M-RIP's UCST phase transition is demonstrated by heating (red) and cooling (blue) cycles at the rate of ± 2 °C.min^{-1}, [M-RIP] = 25 μM (see Figure S9 for representative plots).

To test our hypothesis that the assembly of M-RIP in the IDPP-rich phase is a function of thermal trajectories across the thermodynamic phase boundary, we subjected M-RIP to three distinct thermal treatment processes: direct dissolution without heating or cooling (D), annealing (A), or quenching (Q) schematically shown in the inset of Figure 4a. We then characterized the assemblies using dynamic light scattering (DLS) at identical temperature endpoints (25 °C, below the coexistence curve). We compared both correlation functions

(CRF) and the average hydrodynamic radius (Z_{avg}) at the end points for all three processes, as well as at intermediate temperatures for the annealing process in which the cooling rate of thermal trajectory was compatible with the equilibration times required for DLS measurements.

Comparison of CRFs obtained at the end of each trajectory, D (dotted black line), Q (dashed golden line), and A (solid blue), confirms the pathway dependence of M-RIP assembly. As shown in Figure 4a, the CRF of M-RIP prepared at room temperature (D) *irreversibly* shifted to longer time scales after one cycle of thermal quenching (Q) In both cases, CRFs appeared to exhibit well-defined exponential decay with a single dominant decay time (τ). A similar shift to longer decay time was also observed for the end point of annealing trajectory, but the presence of a distinct shoulder at long decay time, marked with an arrow at $\tau \sim 10^5$ μs, suggests the presence of large aggregates in the solution after annealing. The analysis of CRFs using the method of cumulants, which provides a rough estimate of the hydrodynamic size of assemblies, suggests a similar energy landscape for assemblies (irreversible shift to larger sizes after thermal treatment which depended on the thermal trajectory). RIP remained unassembled (unimers < 10 nm), albeit we also noted the presence of a small population of larger aggregates (>300 nm, Figure S12).

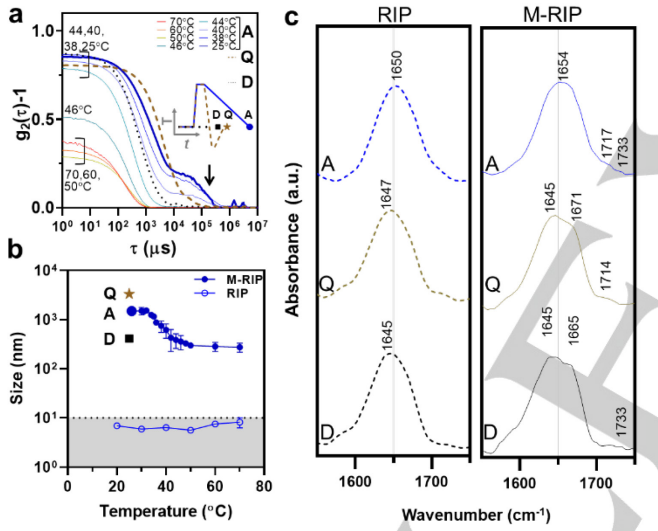

Figure 4. DLS and FT-IR characterization of size and structure of constructs along three user-defined thermal processes: Direct dissolve (D); annealing (A) or quenching (Q): heating above the UCST coexistence curve (70 °C) followed slow annealing (-2°C.min^{-1}) to room temperature or rapid quenching (-20 °C.min^{-1}) to 4 °C, respectively. CRFs (**a**) and the aggregate size (**b**) at the endpoint of process D (dotted), Q (dash), and A (solid) as well as the intermediate temperatures for the annealing pathway. DLS confirms the pathway-dependent assembly of M-RIP. RIP remained unassembled in this temperature range. The arrow added is to emphasize the formation of distinct populations during annealing cycle. The shaded grey area in (b) represents the size regime of unassembled RIP (see Figure S12 for intensity distributions). Error bars indicate the standard deviation of three measurements, [(M-)RIP] = 50 μM. (**c)** The amide I band region of a solution of RIP and M-RIP in D_2O before and after thermal treatment. Myristoylation or the preparation pathway subtly alters the line profile of amide I band (e.g., the location of shoulders and minor peaks). The peak locations are added to aid visual comparison, and the deconvoluted spectra are presented in Figure S14. The grey line in each panel is a visual reference placed at 1650 cm^{-1}, which corresponds to the absorbance of random coils in solution.[31] The spectra are the result of signal averaging of 2-3 measurements, each collected after 128 scans, at 2 cm^{-1} resolution.

Because the amount of scattered light scales with the sixth power of diameter, these aggregates skew the cumulants analysis as Z_{avg} is the intensity weighted harmonic mean size (Figure 4b, grey shaded area). Nonetheless, we did not observe any noticeable change in CRFs or intensity distributions of RIP in this temperature range (20–70 °C, Figures S11 and S12). In contrast, M-RIP assemblies remained in a distinct size range, 200 nm <Z_{avg} < 1500 nm. M-RIP remained assembled even at 70 °C as the observed hydrodynamic size remained an order of magnitude larger than the unimers observed for RIP. These results complement turbidimetry observations as they demonstrate that disappearance of turbidity above T_{cp} is due to a reduction in the size of aggregates below the threshold needed for scattering visible light. As temperature is reduced below 46 °C, the size of the assemblies started to increase, consistent with an increase in the attractive forces between RIP chains at low temperatures, eventually reaching a plateau of 1500 nm around 30 °C. The final Z_{avg} of M-RIP after annealing remained larger than the direct solution process but smaller than what was observed in the quenching process.

To complement the insights derived from light scattering, we used FT-IR to investigate the conformational change in RIP and M-RIP in each pathway (Figure 4c). We chose this technique because, unlike CD and NMR, the acquisition of FT-IR spectra is not hindered by the turbidity and aggregation of protein solution. The differences in the amide I band region of RIP and M-RIP were consistent with subtle differences noted in the spectra of protein powder, albeit the peak location and relative intensities change in D_2O. Notably, the spectrum of RIP shows a single broad peak (~1650 cm^{-1}) in each pathway (D, Q, and A), while the spectral features of M-RIP amide I band change as a function of thermal treatment. Moreover, the peaks above 1700 cm^{-1} (attributed to protonated Asp side chains[32]) are different in the spectra of RIP and M-RIP (consistent with the NMR results) and exhibit subtle pathway-dependent differences for lipidated constructs. We then deconvoluted the amide I band by peak fitting (Figure S14, Table S2) to quantify the observed differences in IR lineshapes. The results show that both myristoylation and the preparative pathway subtly influence the structures and interactions (ionization and H-bonding) of M-RIP. However, we note that the quantitative comparison of deconvolution results requires an assumption that H/D exchange is rapid and quantitative.[33] The disordered nature of the resilin domain (confirmed by CD and FT-IR) supports this assumption, but we remain cognizant that lipid-induced assembly can slow the H/D exchange process, thus affecting the shape and intensity of the amide I band.[31-32, 34]

Having confirmed that M-RIP assembly depends on the thermal processing sequence, we used microscopy to investigate the morphology of M-RIP at the end point of these trajectories (Figure 5). Differential interference contrast (DIC) microscopy was used to visualize the assemblies obtained in the turbid solution at the end of the D pathway (Figure 5a, Figure S15). M-RIP under these conditions formed spherical assemblies resembling protein-rich coacervates reported for other proteins undergoing LLPS.[35] Intriguingly, these droplets were quite round and no structure with an ellipsoidal cross-section was observed. Moreover, they did not exhibit pinching or spreading behavior, and did not fuse or coalesce upon contact, Figure 5a (inset) and Figure S16 for time-lapse DIC).

We used transition electron microscopy (TEM) to image these spherical aggregates at higher resolution. As shown in Figure 5b, these assemblies exhibited similar characteristics (round edges and a lack of fusion between contacting particles) in TEM images. Intriguingly, all spheres (diameter = 988 ± 277 nm, Figure 5c) had uniform contrast, and their cross-sectional area did not change when viewed from different angles (Figure S17). This suggests that M-RIP formed stable microspheres in D pathway that did not collapse onto the surface after drying.

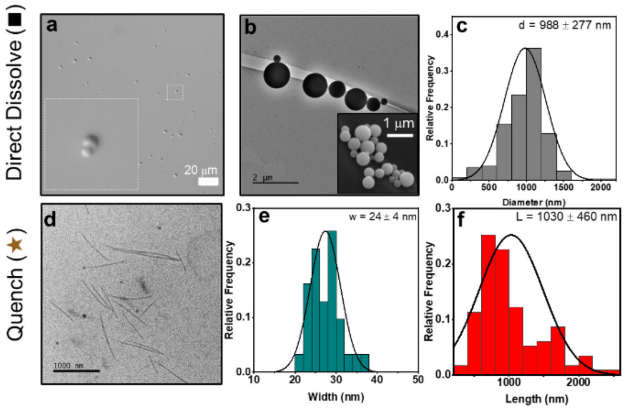

Figure 5. Microscopic characterization of M-RIP assemblies below the UCST coexistence curve at the end of the D (a–c) and Q (d–f) trajectory using DIC and TEM. **(a)** Pathway D led to formation of M-RIP droplets with a solid-like character that did not fuse upon contact at the end of D pathway. **(b)** TEM and SEM (inset) confirm that M-RIP forms microspheres under these conditions, consistent with the results of DIC experiments. **(c)** Size distribution of the microspheres obtained from TEM image analysis. See Figure S15 for size distribution obtained from DIC. See Figure S19 for TEM of RIP control. **(d)** TEM Shows that M-RIP solid microspheres transition to thin fibrils in pathway Q. See Figure S20 for thin fibers formed during annealing pathway. **(e, f)** Width and length distribution for the fibers produced in quenching pathway obtained from TEM image analysis. Measurement results are reported as mean ± SD (N > 50), [M-RIP] = 50 μM (DIC) and 70 μM (TEM).

Scanning electron microscopy (SEM) confirmed the presence of these stable protein-based microspheres on the TEM grid (Figure 5b, inset). These observations, which are in contrast with the behavior of the canonical liquid-like coacervates reported in the literature,[36] suggest that M-RIP forms solid-like droplets with reduced dynamics under the D pathway. This is likely due to the combination of lipid-induced assembly and high charge content of RIP that change the interfacial properties of protein-rich droplets in water (Figure S18).

TEM analysis of pathway A demonstrated the presence of a mixture of microspheres and thin fibers, width 9 ± 2 (Figure S20). However, these fibers did not interact strongly with the uranyl acetate contrast agent and often required imaging under defocused mode to enhance contrast. Finally, consistent with the DLS, TEM confirmed that pathway Q resulted in an irreversible morphological transition in M-RIP assemblies from micro-sphere to fibrils, Figure 5d–f). Although fibrils exhibited narrow dispersity in width (24 ± 4 nm), they were relatively polydisperse in length (1030 ± 460 nm) and had a large persistence length (~19 μm) (Figure S21). These fibrils did not interact with Thioflavin T (Figure S22), which suggests that their cross-sections are likely not amyloid-like.[37]

We were encouraged by the observed morphological transition (microsphere to short fibrils) in pathway Q. Compared to spheres, fibrils have a higher propensity to form higher-order assemblies due to their increased surface-area-to-volume ratio, Moreover, at temperatures below coexistence curve, the overall interaction between M-RIP fibrils are attractive, suggesting that aging of M-RIP fibrils would yield new previously inaccessible higher-order assemblies. To explore this possibility further, we incubated M-RIP fibrils at room temperature (below cloud point) and used TEM to analyze the resulting structures. We observed that M-RIP formed a rich array of higher-order 1D and 2D assemblies after 6–18 h incubation at room temperature (Figure 6). Based on the intermediates observed, we identified twisting (Figure 6a–c) and parallel (Figure 6d-f) packing as two dominant modes of assembly that accounted for the observed rich polymorphism in the final structures. We observed similar structures when the aged solution of M-RIP was analyzed with DIC microscope, suggesting that these self-assembled structures were present in the solution and were not artifacts of TEM sample preparation (Figure S23).

We propose that pathway-dependent assembly of M-RIP is due to distinct temperature-dependence of interactions among RIP, lipid, and water (Figure 7). In pathway D, lipid-induced assembly increases the local concentration of proteins and nucleates the formation of M- RIP droplets, which adopt spherical geometry to minimize interfacial tension. In pathways Q and A, increasing the temperature above UCST phase boundary changes the balance of attractive interactions between RIP/RIP and RIP/water. This

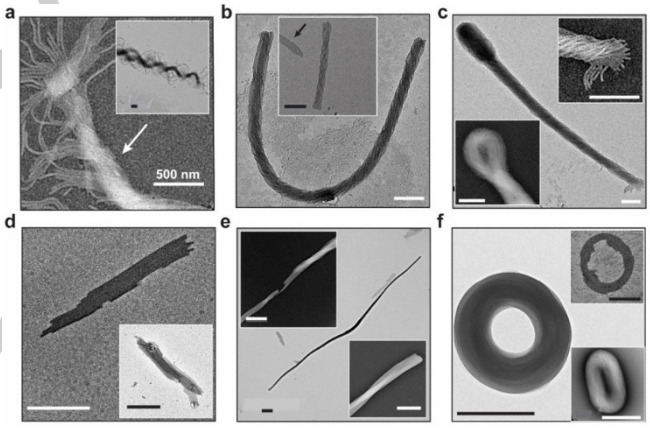

Figure 6. The hierarchical assembly of M-RIP (70 μM) fibrils when incubated below T_{UCST} leads to a rich array of 1D and 2D assemblies. Representative structures of intermediates and products of two dominant assembly modes, twisting (a–c) and parallel assembly (d–f). (**a**) Fibrils (inset) first self-assemble into thin and long threads that associate (twist around each other) to form strands (bundle of threads, white arrow). (**b**) Compact assembly of the strands results in the formation of discrete (1D) braids. The inset contrasts the discrete braids formed via this mechanism with a flat sheet formed via parallel assembly (marked with a black arrow). (**c**) Formation of lasso-like objects via super-coiling (a higher-order 2D assembly) of braids. Bottom inset shows an example of loops formed from the super-coiling of braids. The top inset shows an example of untwisted termini of the braid containing twisted strands. (**d**) Sheets are generated via the lateral assembly of fibers. Multiple sheets can stack on top of each other (inset, three stacked layers). (**e**) Ribbons are produced from the 1D assembly of sheets and exhibited a moderate right-handed twist. The top inset shows the cross-section of a fragmented ribbon formed from the assembly of 5-7 fibers. (**f**) 2D assembly of sheets into toroids. The top inset demonstrates an intermediate of this process in the presence of precursor fibers. The bottom inset is a toroid with ellipsoidal cross-section. All scale bars represent 500 nm. M-RIP is often visualized as positively stained on the TEM image. The images in panel (**a**), insets of panels (**c**), and (**e**) are processed with Fiji black and white image inversion algorithm for better visualization of the details. See Figure S24 for additional TEM images.

alters the dimensions of RIP chains (i.e., expansion of collapsed coils) and their macroscopic solubility (i.e., aggregation). In contrast, the hydrophobic forces between the lipid motifs are less dependent on the temperature. Consequently, as the temperature is increased, M-RIP droplets are solubilized but dominant lipid-lipid interactions will limit the expansion of the disordered protein corona. This interplay between the lipid and protein corona can change the physicochemical properties of assemblies (charge, H-bond, and packing parameter) as a function of temperature, which ultimately controls the morphology of oligomers in each pathway. While more work is needed to fully reveal the molecular changes in oligomers in different pathways, the differences in temperature-dependence of zeta potential of RIP and M-RIP support the proposed mechanism and the interplay between the lipid and charged RIP chains. (Figure S25). We suggest that the rate of cooling modulates the kinetics of phase-separation and the type of structures formed below phase boundary. Rapid quenching favors the formation of short fibrils (kinetic product), while slow annealing results in the formation of long fibers. Below the UCST phase boundary, the multi-valent interactions between RIP chains are reinstated which direct the higher-order assembly of shorter (and more dynamic) fibrils into observed 1D and 2D structures.

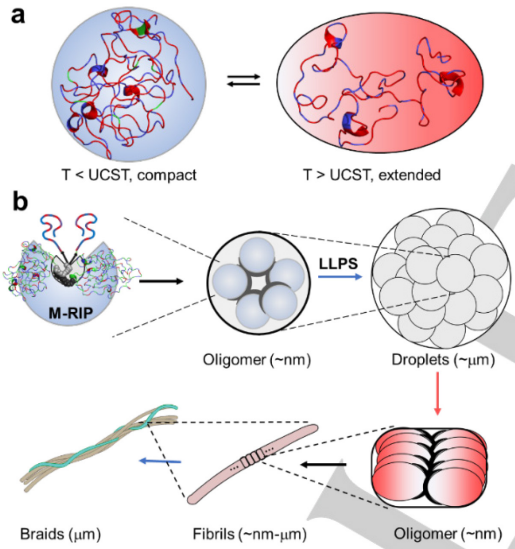

Figure 7. (a) Temperature modulates the molecular interactions and conformations of disordered thermo-responsive proteins such as RIP. **(b)** Proposed mechanism for pathway-dependent assembly of M-RIP.

Conclusion

Our results support the hypothesis that LLPS can be used to encode a programmable response along user-defined thermal processes. The judicious choice of thermal processing methods modulated the balance between competing interactions to control the energy landscape and reach previously inaccessible phase and structural configurations.

Our strategy opens new opportunities for simultaneously controlling the phase behavior and programming of the assembly of protein-based materials. Despite significant progress describing the influence of the physicochemistry of IDPPs (amino acid sequence, length, etc.) on their thermodynamic phase boundary, the design rules to control the kinetics of LLPS at the amino acid level and the outcome of rate-dependent processes such as quenching are not clearly understood.

Cells often use post-translational modifications to control the thermodynamics and kinetics of protein phase separation in vivo.[38] We propose that modification with hydrophobic motifs such as lipids is a promising and untapped chemical design space to tune the material properties of a protein-rich phase. Future work is directed at systematic investigation of the effect of (macro)molecular characteristics (IDPP sequence, and length, lipid type), solution parameters, thermal processing variables (quench depth and rate), and confinement[39] on hierarchical nano- and meso-scale organization of this new class of hybrid materials. We envision an exciting synergy—between high throughput recombinant synthesis of hybrid biopolymers, characterization of both the kinetics and thermodynamics of their phase behavior,[22] and in-situ liquid cell electron microscopy[40]—that can exponentially accelerate the pace of bio-nanomaterials design and discovery. We expect that this strategy will be applicable to other naturally occurring IDPs with UCST behavior,[20e] synthetic polymers,[41] or multi-component hybrid systems[42] and impact the application of this class of biopolymers for the templated synthesis of nanomaterials at extreme temperatures, responsive reactors and engineered protocells.

Acknowledgements

The authors thank Professors Matthew Maye and Dacheng Ren for providing access to the DLS instrument and the DIC microscope. We are thankful to Sweta Roy and Xin Liu for assistance with obtaining DIC and TEM images. This research was generously supported by ACS PRF 61198-DNI, NSF-DMR-BMAT-2105193, Ralph E. Powe Junior Faculty Enhancement award, and Syracuse University (through seed grants from Bioinspired Institute).

Keywords: Protein modifications • phase transitions • Nanotechnology• Supramolecular chemistry• lipoproteins

[1] a. D. Spitzer, L. L. Rodrigues, D. Straßburger, M. Mezger, P. Besenius, *Angew. Chem. Int. Ed.* **2017**, *56*, 15461-15465; b. A. Lampel, S. A. McPhee, H. A. Park, G. G. Scott, S. Humagain, D. R. Hekstra, B. Yoo, P. W. J. M. Frederix, T. D. Li, R. R. Abzalimov, S. G. Greenbaum, T. Tuttle, C. Hu, C. J. Bettinger, R. V. Ulijn, *Science* **2017**, *356*, 1064-1068; c. S. M. Chin, C. V. Synatschke, S. Liu, R. J. Nap, N. A. Sather, Q. Wang, Z. Álvarez, A. N. Edelbrock, T. Fyrner, L. C. Palmer, I. Szleifer, M. Olvera De La Cruz, S. I. Stupp, *Nat. Commun.* **2018**, *9*, 1-11; d. H. W. Schmidt, F. Würthner, *Angew. Chem. Int. Ed.* **2020**, *59*, 8766-8775; e. S. Panja, D. J. Adams, *Chem. Soc. Rev.* **2021**, *50*, 5165-5200; f. N. Bäumer, K. K. Kartha, S. Buss, I. Maisuls, J. P. Palakkal, C. A. Strassert, G. Fernández, *Chem. Sci.* **2021**, *12*, 5236-5245; g. L. MacFarlane, C. Zhao, J. Cai, H. Qiu, I. Manners, *Chem. Sci.* **2021**, *12*, 4661-4682; h. S. Kundu, A. Chowdhury, S. Nandi, K. Bhattacharyya, A. Patra, *Chem. Sci.* **2021**, *12*, 5874-5882; i. Q. Song, A. Kerr, J. Yang, S. Hall, S. Perrier, *Chem. Sci.* **2021**, *12*, 9096-9103; j. S. Sarkar, A. Sarkar, A. Som, S. S. Agasti, S. J. George, *J. Am. Chem. Soc.* **2021**, *143*, 11777-11787; k. A. Sikder, S. Chakraborty, P. Rajdev, P. Dey, S. Ghosh, *Acc. Chem. Res.* **2021**, *54*, 3516-3520; l. O. Shyshov, S. V. Haridas, L. Pesce, H. Qi, A. Gardin, D. Bochicchio, U. Kaiser, G. M. Pavan, M. von Delius, *Nat. Commun.* **2021**, *12*, 1-11; m. M. J. Webber, E. A. Appel, E. W. Meijer, Robert Langer, *Nat. Mater.* **2016**, *15*, 13-26.

[2] S. Panettieri, R. V. Ulijn, *Curr. Opin. Struct. Biol.* **2018**, *51*, 9-18.
[3] D. B. Amabilino, D. K. Smith, J. W. Steed, *Chem. Soc. Rev.* **2017**, *46*, 2404-2420.
[4] a. G. Ghosh, P. Dey, S. Ghosh, *Chem. Commun.* **2020**, *56*, 6757-6769; b. J. Matern, K. K. Kartha, L. Sánchez, G. Fernández, *Chem. Sci.* **2020**, *11*, 6780-6788; c. A. Mishra, D. B. Korlepara, S. Balasubramanian, S. J. George, *Chem. Commun.* **2020**, *56*, 1505-1508; d. M. Wehner, F. Würthner, *Nat. Rev. Chem.* **2020**, *4*, 38-53; e. A. Sarkar, R. Sasmal, A. Das, S. S. Agasti, S. J. George, *Chem. Commun.* **2021**, *57*, 3937-3940.
[5] E. Mattia, S. Otto, *Nat. Nanotechnol.* **2015**, *10*, 111-119.
[6] a. Y. Yan, J. Huang, B. Z. Tang, *Chem. Commun.* **2016**, *52*, 11870-11884; b. J. K. Sahoo, C. G. Pappas, I. R. Sasselli, Y. M. Abul-Haija, R. V. Ulijn, *Angew. Chem. Int. Ed.* **2017**, *56*, 6828-6832; c. R. Alberstein, Y. Suzuki, F. Paesani, F. A. Tezcan, *Nat. Chem.* **2018**, *10*, 732-739; d. M. Kumar, N. L. Ing, V. Narang, N. K. Wijerathne, A. I. Hochbaum, R. V. Ulijn, *Nat. Chem.* **2018**, *10*, 696-703; e. R. K. Grötsch, C. Wanzke, M. Speckbacher, A. Angl, B. Rieger, J. Boekhoven, *J. Am. Chem. Soc.* **2019**, *141*, 9872-9878.
[7] a. J. H. Van Esch, R. Klajn, S. Otto, *Chem. Soc. Rev.* **2017**, *46*, 5474-5475; b. G. Wang, S. Liu, *ChemSystemsChem* **2020**, *2*, e1900046; c. H. Muradyan, Z. Guan, *ChemSystemsChem* **2020**, *2*, e2000024; d. C. Wanzke, A. Jussupow, F. Kohler, H. Dietz, V. R. Kaila, J. Boekhoven, *ChemSystemsChem* **2020**, *2*, e1900044; e. M. Weißenfels, J. Gemen, R. Klajn, *Chem* **2021**.
[8] F. Tantakitti, J. Boekhoven, X. Wang, R. V. Kazantsev, T. Yu, J. Li, E. Zhuang, R. Zandi, J. H. Ortony, C. J. Newcomb, L. C. Palmer, G. S. Shekhawat, M. O. De La Cruz, G. C. Schatz, S. I. Stupp, *Nat. Mater.* **2016**, *15*, 469-476.
[9] a. Y. Tian, F. B. Polzer, H. V. Zhang, K. L. Kiick, J. G. Saven, D. J. Pochan, *Biomacromolecules* **2018**, *19*, 4286-4298; b. M. A. VandenBerg, J. K. Sahoo, L. Zou, W. McCarthy, M. J. Webber, *ACS Nano* **2020**, *14*, 5491-5505.
[10] a. Y. Lin, M. Penna, M. R. Thomas, J. P. Wojciechowski, V. Leonardo, Y. Wang, E. T. Pashuck, I. Yarovsky, M. M. Stevens, *ACS Nano* **2019**, *13*, 1900-1909; b. P. A. Korevaar, C. J. Newcomb, E. Meijer, S. I. Stupp, *J. Am. Chem. Soc.* **2014**, *136*, 8540-8543; c. G. Ghosh, S. Ghosh, *Chem. Commun.* **2018**, *54*, 5720-5723.
[11] a. A. T. Haedler, S. C. Meskers, R. H. Zha, M. Kivala, H.-W. Schmidt, E. W. Meijer, *J. Am. Chem. Soc.* **2016**, *138*, 10539-10545; b. Z. Feng, T. Zhang, H. Wang, B. Xu, *Chem. Soc. Rev.* **2017**, *46*, 6470-6479; c. J. Leira-Iglesias, A. Sorrenti, A. Sato, P. A. Dunne, T. M. Hermans, *Chem. Commun.* **2016**, *52*, 9009-9012; d. S. Ogi, C. Grzeszkiewicz, F. Würthner, *Chem. Sci.* **2018**, *9*, 2768-2773; e. A. Jain, S. Dhiman, A. Dhayani, P. K. Vemula, S. J. George, *Nat. Commun.* **2019**, *10*, 1-9; f. H. Wang, L. Liu, S. Bai, X. Guo, R. Eelkema, J. H. Van Esch, Y. Wang, *Soft Matter* **2020**, *16*, 9406-9409.
[12] a. Z. Chen, Y. Liu, W. Wagner, V. Stepanenko, X. Ren, S. Ogi, F. Würthner, *Angew. Chem. Int. Ed.* **2017**, *56*, 5729-5733; b. J. Tan, L. Zhang, M.-C. Hsieh, J. T. Goodwin, M. A. Grover, D. G. Lynn, *Chem. Sci.* **2021**, *12*, 3025-3031.
[13] E. Sjölander, S. Seifeddine, *J. Mater. Process. Technol.* **2010**, *210*, 1249-1259.
[14] a. K. Kim, M. W. Schulze, A. Arora, R. M. Lewis, M. A. Hillmyer, K. D. Dorfman, F. S. Bates, *Science* **2017**, *356*, 520-523; b. G. N. Kangovi, S. Park, S. Lee, *Macromolecules* **2018**, *51*, 7274-7283.
[15] a. A. C. Dumetz, A. M. Chockla, E. W. Kaler, A. M. Lenhoff, *Biophys. J.* **2008**, *94*, 570-583; b. J. D. Camino, P. Gracia, S. W. Chen, J. Sot, I. de la Arada, V. Sebastián, J. L. Arrondo, F. M. Goñi, C. M. Dobson, N. Cremades, *Chem. Sci.* **2020**, *11*, 11902-11914.
[16] a. M. J. Glassman, B. D. Olsen, *Biomacromolecules* **2015**, *16*, 3762-3773; b. G. Qin, M. J. Glassman, C. N. Lam, D. Chang, E. Schaible, A. Hexemer, B. D. Olsen, *Adv. Funct. Mater.* **2015**, *25*, 729-738; c. C. N. Lam, B. D. Olsen, *Soft Matter* **2013**, *9*, 2393; d. C. E. Mills, Z. Michaud, B. D. Olsen, *Biomacromolecules* **2018**, *19*, 2517-2525; e. S. Roberts, V. Miao, S. Costa, J. Simon, G. Kelly, T. Shah, S. Zauscher, A. Chilkoti, *Nat. Commun.* **2020**, *11*, 1342.
[17] A. George, Y. Chiang, B. Guo, A. Arabshahi, Z. Cai, W. W. Wilson, in *Macromolecular Crystallography Part A*, Elsevier, **1997**, pp. 100-110.
[18] Clifford P. Brangwynne, P. Tompa, Rohit V. Pappu, *Nature Physics* **2015**, *11*, 899-904.
[19] R. L. Baldwin, *Proc. Natl. Acad. Sci. U.S.A.* **1986**, *83*, 8069-8072.
[20] a. G. L. Dignon, W. Zheng, Y. C. Kim, J. Mittal, *ACS Cent. Sci.* **2019**, *5*, 821-830; b. K. M. Ruff, S. Roberts, A. Chilkoti, R. V. Pappu, *J. Mol. Biol.* **2018**, *430*, 4619-4635; c. R. A. Kapelner, A. C. Obermeyer, *Chem. Sci.* **2019**, *10*, 2700-2707; d. B. S. Schuster, G. L. Dignon, W. S. Tang, F. M. Kelley, A. K. Ranganath, C. N. Jahnke, A. G. Simpkins, R. M. Regy, D. A. Hammer, M. C. Good, J. Mittal, *Proc. Natl. Acad. Sci. U.S.A.* **2020**, *117*, 11421-11431; e. B. S. Schuster, E. H. Reed, R. Parthasarathy, C. N. Jahnke, R. M. Caldwell, J. G. Bermudez, H. Ramage, M. C. Good, D. A. Hammer, *Nat. Commun.* **2018**, *9*, 2985; f. Y. Jang, M. C. Hsieh, D. Dautel, S. Guo, M. A. Grover, J. A. Champion, *Biomacromolecules* **2019**, *20*, 3494-3503.
[21] F. G. Quiroz, A. Chilkoti, *Nat. Mater.* **2015**, *14*, 1164-1171.
[22] B. A. Rogers, K. B. Rembert, M. F. Poyton, H. I. Okur, A. R. Kale, T. Yang, J. Zhang, P. S. Cremer, *Proc. Natl. Acad. Sci. U.S.A.* **2019**, *116*, 15784-15791.
[23] a. C. M. Elvin, A. G. Carr, M. G. Huson, J. M. Maxwell, R. D. Pearson, T. Vuocolo, N. E. Liyou, D. C. C. Wong, D. J. Merritt, N. E. Dixon, *Nature* **2005**, *437*, 999-1002; b. R. Balu, R. Knott, N. P. Cowieson, C. M. Elvin, A. J. Hill, N. R. Choudhury, N. K. Dutta, *Scientific Reports* **2015**, *5*, 10896; c. R. Balu, N. K. Dutta, A. K. Dutta, N. R. Choudhury, *Nat. Commun.* **2021**, *12*, 149.
[24] M. Dzuricky, B. A. Rogers, A. Shahid, P. S. Cremer, A. Chilkoti, *Nat. Chem.* **2020**, *12*, 814-825.
[25] E. W. Martin, A. S. Holehouse, I. Peran, M. Farag, J. J. Incicco, A. Bremer, C. R. Grace, A. Soranno, R. V. Pappu, T. Mittag, *Science* **2020**, *367*, 694-699.
[26] a. M. S. Hossain, X. Liu, T. I. Maynard, D. Mozhdehi, *Biomacromolecules* **2020**, *21*, 660-669; b. M. S. Hossain, C. Maller, Y. Dai, S. Nangia, D. Mozhdehi, *Chem. Commun.* **2020**, *56*, 10281-10284; c. D. Mozhdehi, K. M. Luginbuhl, J. R. Simon, M. Dzuricky, R. Berger, H. S. Varol, F. C. Huang, K. L. Buehne, N. R. Mayne, I. Weitzhandler, M. Bonn, S. H. Parekh, A. Chilkoti, *Nat. Chem.* **2018**, *10*, 496-505; d. K. M. Luginbuhl, D. Mozhdehi, M. Dzuricky, P. Yousefpour, F. C. Huang, N. R. Mayne, K. L. Buehne, A. Chilkoti, *Angew. Chem. Int. Ed. Engl.* **2017**, *56*, 13979-13984.
[27] R. E. Lyons, C. M. Elvin, Karin Taylor, Nicolas Lekieffre, J. A.M. Ramshaw, *Biotechnol. Bioeng.* **2012**, *109*, 2947-2954.
[28] M. P. Williamson, *Prog. Nucl. Magn. Reson. Spectrosc.* **2013**, *73*, 1-16.
[29] J. Seuring, S. Agarwal, *Macromol. Rapid Commun.* **2012**, *33*, 1898-1920.
[30] N. K. Dutta, M. Y. Truong, S. Mayavan, N. R. Choudhury, C. M. Elvin, M. Kim, R. Knott, K. M. Nairn, A. J. Hill, *Angew. Chem. Int. Ed. Engl.* **2011**, *50*, 4428-4431.
[31] J. Kong, S. Yu, *Acta. Biochim.* **2007**, *39*, 549-559.
[32] A. Barth, *Prog. Biophys. Mol. Biol.* **2000**, *74*, 141-173.
[33] S. W. Englander, N. W. Downer, H. Teitelbaum, *Annual review of biochemistry* **1972**, *41*, 903-924.
[34] A. Natalello, D. Ami, S. M. Doglia, in *Intrinsically disordered protein analysis*, Springer, **2012**, pp. 229-244.
[35] D. M. Mitrea, B. Chandra, M. C. Ferrolino, E. B. Gibbs, M. Tolbert, M. R. White, R. W. Kriwacki, *J. Mol. Biol.* **2018**, *430*, 4773-4805.
[36] S. Alberti, A. Gladfelter, T. Mittag, *Cell* **2019**, *176*, 419-434.
[37] K. Gade Malmos, L. M. Blancas-Mejia, B. Weber, J. Buchner, M. Ramirez-Alvarado, H. Naiki, D. Otzen, *Amyloid* **2017**, *24*, 1-16.
[38] M. Hofweber, D. Dormann, *J. Biol. Chem.* **2019**, *294*, 7137-7150.
[39] Y. Zong, S.-M. Xu, W. Shi, C. Lu, *Nat. Commun.* **2021**, *12*, 1-10.
[40] H. Wu, H. Friedrich, J. P. Patterson, N. A. Sommerdijk, N. de Jonge, *Adv. Mater.* **2020**, *32*, 2001582.
[41] Z. Zhang, H. Li, S. Kasmi, S. Van Herck, K. Deswarte, B. N. Lambrecht, R. Hoogenboom, L. Nuhn, B. G. De Geest, *Angew. Chem. Int. Ed.* **2019**, *58*, 7866-7872.
[42] H. K. Lau, A. Paul, I. Sidhu, L. Li, C. R. Sabanayagam, S. H. Parekh, K. L. Kiick, *Adv. Sci.* **2018**, *5*, 1701010.

Entry for the Table of Contents

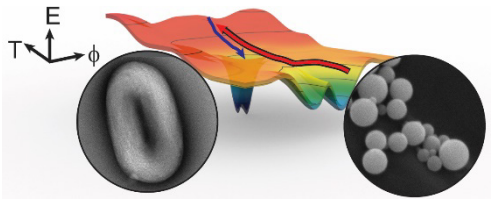

Low-fat high protein recipes for nanosynthesis: Temperature-triggered liquid-liquid phase separation of a lipidated protein is leveraged to direct amphiphilic building blocks across the supramolecular energy landscape. This pathway dependent thermal processing is used to synthesize two-dimensional nanomaterials with complex morphologies such as toroids.